

# Role of scattering in nanotransistors

Alexei Svizhenko and M. P. Anantram

NASA Ames Research Center, Mail Stop: 229-1, Moffett Field, CA 94035-1000.

November 1, 2018

DRAFT

arXiv:cond-mat/0211069v3 [cond-mat.mes-hall] 11 Apr 2003

**Abstract**

We model the influence of scattering along the channel and extension regions of dual gate nanotransistor. It is found that the reduction in drain current due to scattering in the right half of the channel is comparable to the reduction in drain current due to scattering in the left half of the channel, when the channel length is comparable to the scattering length. This is in contrast to a popular belief that scattering in the source end of a nanotransistor is significantly more detrimental to the drive current than scattering elsewhere. As the channel length becomes much larger than the scattering length, scattering in the drain-end is less detrimental to the drive current than scattering near the source-end of the channel. Finally, we show that for nanotransistors, the classical picture of modeling the extension regions as simple series resistances is not valid.

Accepted for publication in "IEEE Transaction in Electron Devices on Electron Devices"

## I. INTRODUCTION

Experimental and theoretical work on nanotransistors has been a hot area of research because of significant advance in lithography. The significant advances in lithography have led to the construction of nanotransistors with channel lengths smaller than 25 nanometers (nm) [1], [2], [3]. It is believed that devices with channel lengths equal to 10 nm may become possible in research laboratories [4]. In these nanotransistors, the length scales of the channel, gate, screening and scattering lengths, begin to become comparable to one another. This is not the case for long channel MOSFETs, where the channel and gate lengths are much larger than the scattering lengths. As a result of the comparable length scales, it is expected that the physics of nanotransistors will begin deviating from that of long channel transistors.

The resistance of a MOSFET (Fig. 1) with a long channel length can be qualitatively thought of as arising in four regions, Extension regions near the source (Ex-s) and drain (Ex-d), Channel (Ch), and Contacts. It is believed that the resistance of the contacts and extension regions are extrinsic series resistances [5], while the channel resistance is intrinsic to the MOSFET. For a given doping distribution, both electrostatics and *scattering* of the current carriers play an important role in determining the drive current. Electrostatics dictates that the total carrier density in a long channel MOSFET is approximately  $C_{ox}(V_G - V_S)$ , where  $V_G$  and  $V_S$  are the gate and source voltages. The role of scattering of current carriers in long channel transistors is modeled using the mobility. For nanotransistors with ultra short channel lengths, there are some deviations in the electrostatics from the long channel case [5]. The role of scattering is however not well understood in nanotransistors. Most work on nanotransistors use the drift diffusion equations which are applicable to long channel MOSFETs or fully ballistic calculations based on the Schroedinger equation. A detailed understanding of the influence of scattering is important as it is crucial in determining the on-current of nanotransistors. The role of scattering is however not straight forward to determine without a calculation because scattering tends to change the carrier and current densities in the channel and extension regions, both spatially and energetically. Further, the physics of this redistribution depends sensitively on the channel and scattering lengths as demonstrated in this paper.

The aim of this paper is to model the exact influence of scattering at different spatial locations along the channel and extension regions of silicon n-MOSFETs. We consider only electron-phonon scattering, which is an important scattering mechanism in devices with undoped channels. References [6] and [7] have recently pointed out that electron-electron and plasmon scattering may play an important role in degrading nanotransistor characteristics. Electron-electron scattering in the drain side will lead to carriers having an energy larger than the source injection barrier. The resulting small tail of hot carriers [8] will be reflected back into the source-end, there by causing an increase in the source injection barrier and a corresponding decrease in drain current. The modeling of these effects and interface roughness is beyond the scope of our current work.

In our calculations, we consider the dual gate MOSFET [9], [10], which is considered to be a promising candidate for nanotransistors. The reason for this is the large on-current and better scaling properties it offers, when compared to bulk-type MOSFETs [11], [12], [13], [14], [15], [16].

The outline of the paper is as follows. In section II, we present our simulation results on the role of scattering in nanotransistors, where we show that scattering is important throughout the device, and not just in the source-end. This is followed by a discussion explaining why drain-end scattering is important in nanotransistors (section III). In section IV, we show that scattering in the extension regions cannot be modeled as simple series resistances. We conclude in section V. All details of our method and approximations are given in the appendix.

## II. WHERE IS SCATTERING IMPORTANT?: SIMULATION RESULTS

Two devices (Fig. 1) are simulated with the following parameters:

Device A (similar to the Purdue dual gate MOSFET [17].): Channel length ( $L_{Ch}$ ) = 10 nm, channel extends from -5 nm to 5 nm, channel thickness ( $T_{Ch}$ ) = 1.5 nm, oxide thickness = 1.5 nm, gate work function = 4.25 eV, doping in the extension regions =  $1 \text{ E}+20 \text{ cm}^{-3}$ , no doping in the channel, drain voltage ( $V_D$ ) = gate voltage ( $V_G$ ) = 0.6 V, and the dielectric constant of the oxide ( $\epsilon_{ox}$ )=3.9.

Device B: Same as Device A, except that  $L_{Ch}$  = 25 nm, channel extends from - 12.5 nm to 12.5 nm and  $V_G$  = 0.56 V. In all simulations involving this device, scattering is included

only in the channel. The gate length is equal to the channel length for both devices A and B. The temperature assumed in all calculations in this paper is 300K.

We first discuss device A. To elucidate the role of scattering in different spatial regions, we calculate the drain current ( $I_D$ ) as a function of the right boundary of scattering,  $Y_{R-Scatt}$ . Scattering is included from the edge of the source extension region (-20 nm) to  $Y_{R-Scatt}$  in Fig. 2. The ballistic current is 1.92 mA/ $\mu$ m, the value at  $Y_{R-Scatt} = -20$  nm. The channel extends from -5 nm to +5 nm. The main points of this figure are:

(i) The decrease in current from the ballistic value due to scattering in the source extension, channel and drain extension regions are 11.5%, 15.5% and 4% respectively. These values point to the well appreciated result that either reducing the length or flaring the source extension region will make a nanotransistor significantly more ballistic.

(ii) The decrease in drain current due to scattering over the entire channel is important. That is, scattering in the right half of the channel (0 nm to 5nm) is almost as important as scattering in the left half of the channel (-5 nm to 0 nm).

(iii) The drain current continues to decrease significantly due to scattering in the drain extension region. An important question is if this decrease is simply a series resistance effect (see section IV).

We now present results for device B, whose channel length is two and a half times larger than device A. The scattering times are nearly the same for the two devices. As a result of the larger channel length, the probability for a carrier to energetically relax is larger. Here, we find that scattering in the left (-12.5 nm to 0 nm) and right (0 nm to 12.5 nm) halves of the channel reduces the drain current by 32% and 15% respectively from the ballistic value, and the over all ballisticity (ratio of *Current with scattering* to *Ballistic current*) is 53% (dashed line of Fig. 4). Again, this points to the importance of scattering in the drain-end.

In lieu of simulating devices with longer channel lengths, we increase the scattering rate of device B. The scattering rate is increased by a factor of five by artificially increasing the values of the deformation potential quoted in reference [18] by a factor of  $\sqrt{5}$ . Note that device B has almost no DIBL and that we self-consistently solve the Green's function and Poisson's equations with the larger deformation potentials. The ballisticity of device

B with the larger scattering rate is 38%, and the current decreases by 60% and 12% of the ballistic value due to scattering in the left and right halves of the channel respectively (solid line of Fig. 4). It is also apparent from Fig. 4 that the effect of scattering on drain current becomes relatively smaller as  $Y_{R-Scatt}$  approaches the drain-end (12.5 nm).

### III. DISCUSSION

The results of section II show that scattering *at all* locations in the channel is important in determining the drain current of nanoscale MOSFETs. We first discuss device A. For device A, the scattering time ( $\hbar/2|Im(\Sigma_{phonon}^r)|$ ) at an energy of  $E_b + 26$  meV is 50 fs and 24 fs in the source and drain-ends respectively. The scattering times are comparable to the semiclassical transit time of 26 fs (Table I). The scattering (11 nm) and channel lengths (10 nm) are hence comparable (Table I). It is interesting to note that for this device, the argument that the energetic redistribution of electrons in the channel to states with kinetic energy in the transport direction well below  $E_b$  will make drain-end scattering ineffective fails.

To understand why drain-end scattering is important for the parameters in device A, it is useful to plot the change in barrier height ( $E_b$ ) with  $Y_{R-Scatt}$ . Fig. 2 shows  $E_b$  as a function of  $Y_{R-Scatt}$ . It is noted that  $E_b$  first decreases and then increases, with increase in  $Y_{R-Scatt}$ . The decrease of  $E_b$  for  $-20$  nm  $< Y_{R-Scatt} < -4$  nm is due to the potential drop in the source extension region arising from the increasing series resistance. Note that the location of the source injection barrier ( $Y_b$ ) is -4 nm (Fig. 3). For  $Y_{R-Scatt} > Y_b$ ,  $E_b$  increases with  $Y_{R-Scatt}$ . The reason for the increase in  $E_b$  are the electrons reflected towards the source from the right of  $Y_b$ . Electrostatics, more or less demands that the charge in the gate should be approximately  $C_{ox}(V_G - V_S)$  [19], [20], like in long channel MOSFETs [5]. So,  $E_b$  floats to higher energies to compensate for the increase in electron density from the reflected electrons. This increase in  $E_b$  contributes significantly to the decrease in the drain current even due to scattering in the right half of channel (0 nm to 5 nm). The increase in  $E_b$  with increase in  $Y_{R-Scatt}$  becomes smaller in the right end of Fig. 2 because the electrons scattered here contribute less significantly to the channel charge, as will be apparent from the discussion below.

We now discuss device B. Device B is different from device A in that its channel length is

two and a half times longer than that of device A. The importance of scattering in the right half of the channel is obvious for device B from the dashed line of Fig. 4. Here, scattering in the left (-12.5 nm to 0 nm) and right (0 nm to 12.5 nm) halves of the channel reduce the drain current by 32% and 15% respectively from the ballistic value. To complement the discussion of device A in terms of  $E_b$ , we will discuss device B in terms of another useful quantity:  $J(Y, E)$ , which is the current distribution as a function of total energy  $E$  at  $Y$ .  $J(Y, E)$  gives us partial information about the energetic redistribution of current due to scattering (see end of current section). When the channel length is comparable to the scattering length,  $J(Y, E)$  is peaked in energy above  $E_b$ , in the right half of the channel (Fig. 5 (a)). Scattering causes reflection of this current towards the source. This is the first reason for the reduction in drain current. The second reason is that the reflected electrons lead to an increase in the channel electron density (classical MOSFET electrostatics). As the charge in the channel should be approximately  $C_{ox}(V_G - V_S)$ , the source injection barrier  $E_b$  floats to higher energies to compensate for the reflected electrons. The increase in  $E_b$  leads to a further decrease in drain current due to scattering in the right half of the channel.

To gain further insight into the role of carrier relaxation, we now discuss device B when the scattering length is five times smaller. The scattering length  $L_{scatt}$  is defined in Table I. Scattering in the right half of the channel for  $L_{scatt} = 2.2$  nm is significantly less detrimental to the drain current relative to scattering in the left half of the channel, when compared to the device with  $L_{scatt} = 11$  nm. As  $L_{Ch}$  (25 nm) is much larger than  $L_{scatt}$  (2.2 nm), multiple scattering events now lead to an energy distribution of current that is peaked well below the source injection barrier in the right half of the channel as shown in Fig. 5 (b). The first moment of energy (mean) with respect to the current distribution function, which is defined by  $\frac{\int dE E J(Y, E)}{\int dE J(Y, E)}$ , is also shown in Fig. 5. This mean also shows that the carriers relax in a manner akin to bulk MOSFETs as a function of  $Y$  in Fig. 5 (b). Carriers reflected in the right half of the channel can no longer reach  $Y_b$  due to the large barrier to the left, and so contribute less significantly to the charge density. Thus, explaining the diminished influence of scattering in the right half of the channel relative to the left half of the channel, for devices with the channel length much larger than the

scattering length.

The above discussion would be incomplete without discussing the electrostatic potential profiles, with and without scattering. The solid line in Fig. 6 is the electrostatic potential in the ballistic limit. Increasing  $Y_{R-Scatt}$  from - 2.5 nm to 2.5 nm causes  $E_b$  to increase because of carriers reflected towards the source. Further increase in  $Y_{R-Scatt}$  to 7.5 nm causes very little increase in  $E_b$  because scattering in the right half of the channel is less effective in changing the channel electron density. The electrostatic potential changes appreciably to the right of  $Y_b$  due to scattering. It is also interesting to note that the electrostatic potential drop for  $Y_{R-Scatt} = 7.5$  nm is linear to the right of  $Y_b$  compared to the ballistic case because of scattering in the channel.

We now comment briefly on two issues:

- The quantity  $E_b - 2kT$  that has been discussed before in references [17] and [21].
- The influence of elastic scattering without any inelastic scattering.

For devices A and B, the potential profile in the right half of the channel is well below  $E_b - 2kT$ . Yet, scattering in the right half of the channel is detrimental to drain current, relative to scattering in the left half of the channel. The reason for this are the hot electrons in the right half of the channel that are reflected to the source-end /  $Y_b$ . However, if the scattering rate in the left half of the channel is large enough to energetically relax the electrons to energies comparable to  $E_b - 2kT$ , then the scattering of these electrons in the drain-end are relatively less detrimental to the reduction in drain current because the carriers cannot easily gain an energy of few times the thermal energy. This phenomenon of the diminished role of scattering in the channel at the drain-end relative to the source-end because of thermalized carriers is seen in Fig. 4 (solid line).

In the presence of elastic scattering processes such as interface roughness scattering, the electron does not loose total energy. However, the kinetic energy in the transport direction can diminish at the expense of a corresponding gain in  $\frac{\hbar^2 k_z^2}{2m_z^*}$ . The additional density of states for scattering that is available in the drain-end in comparison to the source-end will also make drain-end scattering less effective than source-end scattering. While we included such process in our calculations, the quantity  $J(Y, E)$  captures only the effect of change in total energy. A physically motivated study quantifying the relative roles of elastic and



inelastic scattering will be a useful future study.

#### IV. FAILURE OF THE CLASSIC SERIES RESISTANCE PICTURE FOR NANOTRANSISTORS

We ask the question if scattering in the extension regions is a simple series resistance. The classic series resistance picture [5] relates the current in a device with long extension regions to the current in the same device without (or with much smaller) extension regions. The relationship is particularly simple for the case where the series resistance in the source extension region is negligible [5],

$$I_D^{scatt}(V_D) \sim I_D^{noscat}(V_D - \delta V_D) , \quad (1)$$

where,  $I_D^{scatt}(V_D)$  and  $I_D^{noscat}(V_D - \delta V_D)R_D$  are the drain currents with and without scattering in the drain extension region, at drain biases of  $V_D$  and  $V_D - \delta V_D$  respectively.  $\delta V_D = I_D^{scatt}(V_D)R_D$ , is the electrostatic potential drop in the drain extension region, which has a series resistance of  $R_D$ . To answer the question on the appropriateness of the classic series resistance picture, we consider a case where the channel and source extension region are ballistic. Scattering is introduced only in the drain extension region with deformation potentials that are  $\sqrt{5}$  times larger than in silicon (scattering time is 5 times smaller).

Fig. 7 shows the decrease in drain current with  $Y_{R-Scatt}$ . The striking point of Fig. 7 is the super-linear decrease of drain current. The  $I_D(V_D)$  curves (inset of Fig. 7) predict a significantly smaller decrease in drain current with increase in  $Y_{R-Scatt}$  when Eq. 1 is used. It is helpful to estimate the drain current from Eq. 1 and compare it to the calculated value. For Device A in Fig. 7, the voltage drop in the drain extension region with scattering is approximately 100 mV (plot not shown). Now, if Eq. 1 is used to estimate the drain current with scattering in the drain extension region and if we take  $\delta V_D = 200$  mV, which is larger than the estimated 100 mV, then we find the drain current to be 1.83 mA/ $\mu\text{m}$  (inset of Fig. 7). The calculated drain current is however much lower at 1.38 mA/ $\mu\text{m}$ !

The physics of the large reduction in drain current for the smaller values of  $Y_{R-Scatt}$  is essentially that discussed in section III: When scattering in the channel does not effectively thermalize carriers, the current distribution is peaked at energies above  $E_b$ , upon carriers exiting the channel. Scattering in the drain extension region then causes reflection of

electrons towards the source-end. As a result,  $E_b$  increases so as to keep the electron density in the channel approximately  $C_{ox}(V_G - V_S)$ . The drain current decreases dramatically as a result of the increase in  $E_b$ . Admittedly, this argument in terms of  $C_{ox}(V_G - V_S)$  is over simplified but it seems to capture the essential point. The main point is that if carriers are not relaxed upon exiting the channel (as would be the case for nano-transistors), then, the drain extension region cannot be modeled by a simple series resistance. That is, Eq. (1) fails for nano-transistors where the channel length is comparable to the scattering length. The effect of the drain extension region in causing a reduction in drain current would be small in the following cases:

(i) The channel is much longer than the scattering length such that the carriers exiting the channel at the drain-end are energetically relaxed / thermalized. Then, the modeling of the drain extension region as a simple series resistance would be appropriate. This is seen in the right end of Fig. 7, where, upon sufficient relaxation of electrons, the decrease in current with increase in  $Y_{R-Scatt}$  becomes much smaller.

(ii) The drain extension region rapidly flares out. Then, the probability for a scattered electron to return to the source-end will be small due to the larger number of modes available in the drain extension region. A careful analysis on how fast the drain extension region flares out should also take into account the role of the Miller effect.

## V. CONCLUSIONS

In conclusion, we find that the potential profile, channel and scattering length scales play an important role in determining the *relative* importance of scattering at different locations along the channel of a nanotransistor. In devices where the channel length is comparable to the scattering length, the role of scattering in the drain-end (right half of the channel) is comparable to the role of scattering in the source-end (left half of the channel), in reducing the drain current (Fig. 2 and dashed line of Fig. 4). This is contrary to a belief that scattering is significantly more important in the source-end of the device. The reason for the detrimental role of scattering in the drain-end are the hot carriers in the drain-end. When the channel length is much larger than the scattering length, then scattering in the source-end becomes relatively more important than scattering in the drain-end (solid line of Fig. 4). In this case, we stress that it is the energetic redistribution of carriers due to

scattering in the source-end to energies below the source injection barrier ( $E_b$ ) that makes scattering in the drain-end relatively less detrimental to the drain current.

The classical series resistance picture for modeling the narrow extension regions fail for nanotransistors. The reason for this failure are the hot carriers entering the drain extension region. A straight forward option to enable the usage of the series resistance picture is to push the region treated as a drain series resistance further to the right, such that all carriers entering this region are energetically relaxed. A more interesting option of altering the classical series resistance picture to account for the hot carriers in the drain end of nanotransistors was not considered in this paper.

The relative importance of scattering in the drain-end of nanotransistors, where the channel length is comparable or smaller than the scattering length, points to the importance of making the extension regions small. Long extension regions in nanotransistors will affect the performance (drive current) much more adversely than in long channel transistors.

## APPENDIX

The approach consists of solving the nonequilibrium Green's function and Poisson's equations. The effective mass Hamiltonian considered is,

$$H = \sum_b -\frac{\hbar^2}{2} \left[ \frac{d}{dx} \left( \frac{1}{m_x^b} \frac{d}{dx} \right) + \frac{d}{dy} \left( \frac{1}{m_y^b} \frac{d}{dy} \right) + \frac{d}{dz} \left( \frac{1}{m_z^b} \frac{d}{dz} \right) \right] + V(x, y), \quad (2)$$

where  $(m_x^b, m_y^b, m_z^b)$  are the (x, y, z) components of the effective mass in valley  $b$  of silicon, and the potential does not vary in the  $z$  direction. The gate oxides are treated as hard walls, the channel is extremely narrow (1.5 nm), the drain and gate biases are smaller than 0.7 V, and the dual gate FET is perfectly symmetric in the  $X$ -direction of Fig. 1. The first three subband energy levels in the source extension region are approximately equal to 173 meV, 691 meV (both due to  $m_y = 0.98m_0$ ) and 891 meV (due to  $m_y = 0.19m_0$ ) above the bulk conduction band. The Fermi energy of bulk silicon at the doping density considered ( $1\text{E}+20 \text{ cm}^{-3}$ ) is approximately 60 meV above the conduction band. For the doping density considered, electrons are primarily injected from the source into the first subband. At the drain end, more than one energy level can in principle contribute to current. As only a few subbands are populated, we model transport in these subbands in an approximate way using the 1D Schroedinger equation as outlined below. We find the

spatially dependent subband energies  $E_n(y)$  by solving Schroedinger's equation at each  $y$ -cross section ( $y$  is only a parameter),

$$\left[ -\frac{\hbar^2}{2m_x^b} \frac{d}{dx} \left( \frac{1}{m_x^b} \frac{d}{dx} \right) + V(x, y) \right] \Psi_n(x, y) = E_n(y) \Psi_n(x, y) . \quad (3)$$

$n = \nu, b$ , where  $\nu$  and  $b$  represent the quantum number due to quantization in the X-direction and the valley respectively. The valley indices  $b$  are required in the calculations of the self-energies for scattering as will be discussed below. In our calculation, we typically retain only the three lowest energy levels. Coupling between the subbands is neglected except via phonon coupling. For the device dimensions and voltages considered, reference [22] found the approximation of considering decoupled subbands to hold good for ultra thin body phase coherent MOSFETs. We solve the following equations for the Green's functions,

$$\left[ E - \frac{\hbar^2 k_z^2}{2m_z^n} - \left( -\frac{\hbar^2}{2} \frac{d}{dy} \left( \frac{1}{m_y^n} \frac{d}{dy} \right) + E_n(y) \right) \right] G_n^r(y, y', k_z, E) - \int dy_1 \Sigma_n^r(y, y_1, k_z, E) G_n^r(y_1, y', k_z, E) = \delta(y - y') , \text{ and} \quad (4)$$

$$\left[ E - \frac{\hbar^2 k_z^2}{2m_z^n} - \left( -\frac{\hbar^2}{2} \frac{d}{dy} \left( \frac{1}{m_y^n} \frac{d}{dy} \right) + E_n(y) \right) \right] G_n^\alpha(y, y', k_z, E) - \int dy_1 \Sigma_n^r(y, y_1, k_z, E) G_n^\alpha(y_1, y', k_z, E) = \int dy \Sigma_n^\alpha(y, y_1, k_z, E) G_n^\alpha(y_1, y', k_z, E) , \quad (5)$$

where,  $\alpha \in >, <$ .  $m_y^n$  and  $m_z^n$  are the effective masses of silicon in the  $y$  and  $z$  directions that give rise to subband index  $n$ .

The self-energies,  $\Sigma_n^{r,>,<}$  can be written as,

$$\Sigma_n^\alpha = \Sigma_{n,C}^\alpha + \Sigma_{n,Phonon}^\alpha, \text{ where} \quad (6)$$

$$\Sigma_{n,Phonon}^\alpha = \Sigma_{n,el}^\alpha + \Sigma_{n,inel}^\alpha . \quad (7)$$

$\Sigma_{n,C}^\alpha$  is the self-energy due to the leads. The phonon self-energy  $\Sigma_{n,Phonon}^\alpha$  consists of two terms,  $\Sigma_{n,el}^\alpha$  due to elastic and  $\Sigma_{n,inel}^\alpha$  due to inelastic scattering. The self-energy due to the leads is non zero only at the first (source) and last (drain) grid points because gate tunneling is neglected.

The following common approximations to calculate the phonon self-energies are used: (i) Phonon scattering is treated only within the self-consistent Born approximation, (ii) The

phonon bath is assumed to always be in equilibrium, and so their occupation numbers are given by the Bose-Einstein distribution function with a spatially independent temperature. (iii) The correlation between subbands  $n$  and  $n'$  ( $\neq n$ ) are neglected. (iv) Scattering due to phonons is assumed to be isotropic. That is, the scattering rate from  $(k_z, E)$  to  $(k'_z, E')$  does not depend on  $k_z$  and  $k'_z$ . This approximation is computationally advantageous because the self-energies due to phonon scattering appear only as diagonal terms in Eqs. 4 and 5. One can derive from these assumptions that the self-energies due to electron-phonon scattering at grid point  $y_i$  are given by [23], [24],

$$\Sigma_{el,n}^\alpha(y_i, E) = \sum_{n'} D_{n,n'}^{el} \frac{\sqrt{m_z^{n'}}}{\pi \hbar \sqrt{2}} \int dE_z \frac{1}{\sqrt{E_z}} G_{n'}^\alpha(y_i, E_z, E), \quad (8)$$

$$\begin{aligned} \Sigma_{inel,n}^<(y_i, E) &= \sum_{n',\eta} D_{n,n'}^{i,\eta} \frac{\sqrt{m_z^{n'}}}{\pi \hbar \sqrt{2}} \int dE_z \frac{1}{\sqrt{E_z}} \\ &[n_B(\hbar\omega_\eta) G_{n'}^<(y_i, E_z, E - \hbar\omega_\eta) + (n_B(\hbar\omega_\eta) + 1) G_{n'}^>(y_i, E_z, E + \hbar\omega_\eta)] , \end{aligned} \quad (9)$$

and

$$\begin{aligned} \Sigma_{inel,n}^>(y_i, E) &= \sum_{n',\eta} D_{n,n'}^{i,\eta} \frac{\sqrt{m_z^{n'}}}{\pi \hbar \sqrt{2}} \int dE_z \frac{1}{\sqrt{E_z}} \\ &[n_B(\hbar\omega_\eta) G_{n'}^>(y_i, E_z, E + \hbar\omega_\eta) + (n_B(\hbar\omega_\eta) + 1) G_{n'}^<(y_i, E_z, E - \hbar\omega_\eta)] . \end{aligned} \quad (10)$$

$\alpha \in >, <, r$  in Eq. 8,  $\eta$  represents the phonon modes, and the square of the matrix elements for phonon scattering are given by,

$$D_{n,n'}^{el} = (\delta_{\nu,\nu'} + \frac{1}{2}) \delta_{b,b'} \frac{D_A^2 kT}{\rho v^2} \quad (11)$$

$$D_{n,n'}^{i,\eta} = (\delta_{\nu,\nu'} + \frac{1}{2}) \left[ \delta_{b,b'} \frac{D_{g\eta}^2 \hbar}{2\rho\omega_{g\eta}} + (1 - \delta_{b,b'}) \frac{D_{f\eta}^2 \hbar}{\rho\omega_{f\eta}} \right] \quad (12)$$

The contribution to elastic scattering is only from acoustic phonon scattering. The values of the deformation potential,  $D_A$ ,  $D_{g\eta}$  and  $D_{f\eta}$ , and phonon frequencies  $\omega_{g\eta}$  and  $\omega_{f\eta}$  are taken from [18].  $\rho$  is the mass density,  $k$  is the Boltzmann constant,  $T$  is the temperature and  $v$  is the velocity of sound.  $b$  and  $b'$  are indices representing the valley. The following scattering processes are included: acoustic phonon scattering in the elastic approximation and g-type intervalley scattering with phonon energies of 12, 19 and 62 meV. It was verified

that f-type (19, 47 and 59 meV phonon) intervalley scattering did not significantly change our results and conclusions. This can be rationalized by noting that f-type intervalley scattering involves subbands with energies higher than the lowest subband. In the regions, where scattering was not included, the deformation potential was set equal to zero.

$\Sigma_{inel,n}^r$  can be obtained using the Kramers-Kronig relationship,

$$Re \left[ \Sigma_{inel,n}^r(y_i, E) \right] = \frac{1}{\pi} P \int dE' \frac{Im \left[ \Sigma_{inel,n}^r(y_i, E') \right]}{E' - E} \text{ and} \quad (13)$$

$$Im \left[ \Sigma_{inel,n}^r(y_i, E) \right] = \frac{1}{2i} \left[ \Sigma_{inel,n}^>(y_i, E) - \Sigma_{inel,n}^<(y_i, E) \right], \quad (14)$$

where  $P$  stands for the principal part of the integral. Note that the self-energies due to electron-phonon scattering depend only on the total energy  $E$  (and not on  $k_z$ ) due to the assumption of isotropic scattering.

The self-energy due to phonon scattering, has real and imaginary parts, both of which vary with energy. The imaginary part of the electron-phonon self-energy which is central to our calculations is responsible for scattering induced broadening of energy levels and energetic redistribution of carriers. The real part of the self-energy which contributes to the shift of the quasi-particle energy levels, appears as a real potential (like the electrostatic potential) in the Green's function equations (Eqs. 4 and 5). To evaluate the importance of the real part of the self-energy in our calculations, we performed simulations with acoustic phonon scattering in silicon, with and without the real part of the self-energy included. We find that the drive current calculated with the real part of the self-energy set to zero in general agrees to within 2 percent of the current calculated with the real part of the self-energy included. This result is not totally surprising because MOSFET electrostatics tends to shift the potential profile appropriately to determine the correct charge under the gate. In the calculations presented in this paper, the real part of the self-energy is set to zero.

In the numerical solution, we consider  $N$  uniformly spaced grid points in the  $Y$ -direction with the grid spacing equal to  $\Delta y$ . The discretized form of Eqs. 4 and 5 are:

$$A_{i,i} G_n^r(y_i, y'_i, k_z, E) + A_{i,i+1} G_n^r(y_{i+1}, y'_i, k_z, E) + A_{i,i-1} G_n^r(y_{i-1}, y'_i, k_z, E) = \frac{\delta_{i,i'}}{\Delta y}, \text{ and} \quad (15)$$

$$A_{i,i} G_n^\alpha(y_i, y'_i, k_z, E) + A_{i,i+1} G_n^\alpha(y_{i+1}, y'_i, k_z, E) + A_{i,i-1} G_n^\alpha(y_{i-1}, y'_i, k_z, E) =$$

$$\Sigma_n^\alpha(y_i, E)G_n^a(y_i, y'_i, k_z, E) , \quad (16)$$

where,

$$A_{i,i} = E - \frac{\hbar^2 k_z^2}{2m_z^n} - \frac{\hbar^2}{m_y^n \Delta y^2} - E_n(y_i) - \Sigma_n^r(y_i, k_z, E) \text{ and} \quad (17)$$

$$A_{i\pm 1,i} = + \frac{\hbar^2}{2m_z^n \Delta y^2} \quad (18)$$

The self-energy due to the source and drain leads contribute only to grid point 1 (left end of the source extension region) and grid point N (right end of the drain extension region), and are given by [25]:  $\Sigma_{n,C}^r(y_1, k_z, E) = (\frac{\hbar^2}{2m_z^n \Delta y^2})^2 g_s(k_z, E)$ ,  $\Sigma_{n,C}^r(y_N, k_z, E) = (\frac{\hbar^2}{2m_z^n \Delta y^2})^2 g_d(k_z, E)$ ,  $\Sigma_{n,C}^<(y_1, k_z, E) = -2i\text{Im}(\Sigma_{n,C}^r(y_1, k_z, E))f_s(E)$ ,  $\Sigma_{n,C}^<(y_N, k_z, E) = -2i\text{Im}(\Sigma_{n,C}^r(y_N, k_z, E))f_d(E)$ ,  $\Sigma_{n,C}^>(y_1, k_z, E) = 2i\text{Im}(\Sigma_{n,C}^r(y_1, k_z, E))[1 - f_s(E)]$ , and  $\Sigma_{n,C}^>(y_N, k_z, E) = 2i\text{Im}(\Sigma_{n,C}^r(y_N, k_z, E))[1 - f_d(E)]$ , where  $y_1$  and  $y_N$  are the left (source-end) and right (drain-end) most grid points respectively,  $g_s(k_z, E)$  and  $g_d(k_z, E)$  are the surface Green's functions of the source and drain leads respectively, and  $f_s$  and  $f_d$  are the Fermi functions in the source and drain contacts respectively.

The non equilibrium electron and current densities are calculated in both the channel and extension regions using the algorithm for  $G^<$  in [26], which avoids full inversion of the  $A$  matrix. For completeness, we state the expressions for the electron and current densities used [26],

$$n_n(y_i, k_z, E) = -iG_n^<(y_i, y_i, k_z, E) \quad (19)$$

$$J_n(y_i, k_z, E) = \frac{e}{\hbar} \sum_n \frac{\hbar^2}{2m_y^n \Delta y^2} [G_n^<(y_i, y_{i+1}, k_z, E) - G_n^<(y_{i+1}, y_i, k_z, E)] . \quad (20)$$

Note that Eqs. 19 and 20 do not include spin and valley degeneracies. The total electron and current densities at grid point  $y_i$  are given by,

$$n(y_i) = 2 \sum_n \frac{\sqrt{m_z^{n'}}}{\pi \hbar \sqrt{2}} \int \frac{dE}{2\pi} \int dE_z \frac{1}{\sqrt{E_z}} n_n(y_i, E_z, E) \quad (21)$$

$$J(y_i) = 2 \sum_n \frac{\sqrt{m_z^{n'}}}{\pi \hbar \sqrt{2}} \int \frac{dE}{2\pi} \int dE_z \frac{1}{\sqrt{E_z}} J_n(y_i, E_z, E) , \quad (22)$$

where the prefactor of 2 in the above equations account for two fold spin degeneracy. While the transport equations are solved in one dimension, we solve Poisson's equation

in two dimensions. The two dimensional electron density used in Poisson's equation is computed from Eqs. (3) and (19) using,

$$n(x_i, y_i, k_z, E) = n_n(y_i, k_z, E)|\Psi_n(x_i, y_i)|^2. \quad (23)$$

The boundary conditions to Poisson's and Green's function equations are applied at the ends of the source and drain extension regions (left and right ends of the source and drain extension regions shown in Fig. 1). In solving the the Green's function and Poisson's equation, note that an applied bias corresponds to a difference in the Fermi levels used in the source and drain regions. The electrostatic potential at the left and right most grid points of the source and drain extension regions respectively are calculated self consistently using the boundary conditions.

Finally, we make a comment on the need for solving quantum mechanical equations to capture the essential effect of hot carriers, described in this paper. The phase of the electron is not central to the physics described in our paper (though the exact value of the drain current depends on it). In calculating the drain current, the quantum mechanical effects of quantization in the X-direction and tunneling along the Y-direction (Fig. 1) can be accounted for semiclassically. So, we feel that a method such as the Monte Carlo method approach to nanotransistors [27], which keeps track of the details of the energetic redistribution of electrons at various spatial locations, will well describe many aspects of the role of scattering.

## REFERENCES

- [1] J. Kedzierski, P. Xuan, V. Subramanian, J. Bokor, T-J King, C. Hu, and E. Anderson. A 20 nm gate-length ultra-thin body p-mosfet with silicide source/drain. *Superlattices and Microstructures*, 28:445–52, 2000.
- [2] A. Hokazono et. al. 14 nm gate length cmosfets utilizing low thermal budget process with poly-sige and ni salicide. In *International Electron Devices Meeting. Technical Digest*, pages 639–42. IEEE , Piscataway, NJ, USA, 2002.
- [3] F. Boeuf. 16 nm planar nmosfet manufacturable within state-of-the-art cmos process thanks to specific design and optimisation. In *International Electron Devices Meeting. Technical Digest*, pages 637–640. IEEE , Piscataway, NJ, USA, 2001.
- [4] B. Yu et. al. Finfet scaling to 10 nm gate length. In *International Electron Devices Meeting. Technical Digest*, pages 251–4. IEEE , Piscataway, NJ, USA, 2002.
- [5] Y. Taur and T. H. Ning. *Fundamentals of Modern VLSI Devices*. Cambridge University Press, 1998.
- [6] M. Fischetti and S. Laux. Long-range coulomb interactions in small si devices. part 1: Performance and reliability. *J. Appl. Phys.*, 89:1205–1231, 2001.



- [7] M. Fischetti. Long-range coulomb interactions in small si devices. part 2: Effective electron mobility in thin-oxide structures. *J. Appl. Phys.*, 89:1232–1250, 2001.
- [8] M. Fischetti and S. Laux. Monte carlo study of sub-bandgap impact ionization in silicon field-effect transistors. In *IEDM Tech. Dig.*, page 305, 1995.
- [9] R.-H. Yan, A. Ourmazd, K. F. Lee, D. Y. Jeon, C. S. Rafferty, and M. R. Pinto. Scaling the si metal-oxide-semiconductor field-effect transistor into the 0.1  $\mu\text{m}$  regime using vertical doping engineering. *Appl. Phys. Lett.*, 59:3315–3317, 1991.
- [10] D. J. Frank, S. E. Laux, and M. Fischetti. Monte carlo simulation of a 30 nm dual-gate mosfet: How short can si go? In *IEDM Technical Digest*, pages 553–556, 1992.
- [11] Y. Taur, D. A. Buchanan, W. Chen, D. J. Frank, K. E. Ismail, S.-H. Lo, G. A. Sai-Halasz, R. G. Viswanathan, H.-J. C. Wann, S. J. Wind, and H.-S. Wong. CMOS scaling into the nanometer regime. *Proc. of the IEEE*, 85:486–504, 1997.
- [12] H.-S. P. Wong, K. K. Chan, and Y. Taur. Self-aligned (top and bottom) double-gate mosfet with a 25 nm thick silicon channel. In *IEDM Technical Digest*, pages 427–430, 1997.
- [13] F. G. Pikus and K. K. Likharev. Nanoscale field-effect transistors: An ultimate size analysis. *Appl. Phys. Lett.*, 71:3661–3663, 1997.
- [14] Z. Ren, R. Venugopal, S. Datta, M. Lundstrom, D. Jovanovic, and D. J. Fossum. The ballistic nanotransistor: a simulation study. In *IEDM Technical Digest*, pages 715–718, 2000.
- [15] L. Chang, S. Tang, T.-J. King, J. Bokor, and C. Hu. Gate length scaling and threshold voltage control of double-gate mosfets. In *IEDM Technical Digest*, pages 719–722, 2000.
- [16] J. R. Watling et. al. *Preprint*.
- [17] Z. Ren and M. S. Lundstrom. Essential physics of carrier transport in nanoscale mosfets. *IEEE TED*, 49:133–141, 2002.
- [18] M. S. Lundstrom. *Fundamentals of carrier transport*. Addison-Wesley Publishing Company, 1990.
- [19] K. Natori. Ballistic metal-oxide-semiconductor field effect transistor. *J. Appl. Phys.*, 76:4870, 1994.
- [20] M. S. Lundstrom. Elementary scattering theory of the mosfet. *IEEE Elec. Dev. Lett.*, 18:361–363, 1997.
- [21] P. J. Price. Monte carlo calculation of electron transport in solids. *Semiconductor and Semimetals*, 14:249–308, 1979.
- [22] R. Venugopal, Z. Ren, S. Datta, M. S. Lundstrom, and D. Jovanovic. Simulating quantum transport in nanoscale transistors: Real versus mode-space approaches. *J. Appl. Phys.*, 92:3730–3739, 2002.
- [23] G. D. Mahan. Quantum transport equation for electric and magnetic fields. *Physics Reports*, 145:251, 1987.
- [24] R. Lake, G. Klimeck, R. C. Bowen, and D. Jovanovic. Single and multiband modeling of quantum electron transport through layered semiconductor devices. *J. Appl. Phys.*, 81:7845, 1997.
- [25] S. Datta. *Electronic Transport in Mesoscopic Systems*. Cambridge University Press, 1997.
- [26] A. Svizhenko et al. Two dimensional quantum mechanical modeling of nanotransistors. *J. of Appl. Phys.*, 91:2343–2354, 2002.
- [27] M. V. Fischetti and S. E. Laux. Monte carlo study of electron transport in silicon inversion layers. *Phys. Rev. B*, 48:2244, 1993.

### Figure Captions:

**Fig. 1:** Schematic of a Dual Gate MOSFET (DG MOSFET). Ex-s and Ex-d are the extension regions and the hatched region is the channel. The white region between the source / drain / channel and gate is the oxide. The device dimension normal to the page is infinite in extent.

**Fig. 2:** Plot of drain current ( $I_D$ ) versus the right boundary of scattering ( $Y_{R-Scatt}$ ) for device A. The scattering time is comparable to the transit time through the channel. Scattering is included from -20 nm to  $Y_{R-Scatt}$ . Note that scattering in the right half of the channel (0 nm to 5 nm), which is to the right of the ' $k_B T$  layer', is almost as deleterious to current flow as scattering in the left half of the channel (-5 nm to 0 nm). The black crosses represent  $E_b$  as a function of  $Y_{R-Scatt}$ . Inset: Ballistic  $I_D$  versus  $V_D$  for  $V_G = 0.6$  V, showing substantial DIBL. Scattering is included both in the channel and extension regions.

**Fig. 3:** Energy of the lowest subband ( $E_1$ ) versus  $Y$  for device A in the ballistic limit.  $E_b$  and  $Y_b$  are the energy and position of the source injection barrier respectively. Potential  $= -\frac{E_1}{e}$ .

**Fig. 4:** Plot of drain current versus  $Y_{R-Scatt}$  for device B. Scattering is included from -12.5 nm to  $Y_{R-Scatt}$ . For  $L_{scatt} = 11$  nm (dashed line) and 2.2 nm (solid line), the effect of scattering in the right half of the channel (0 nm to 12.5 nm) corresponds to nearly a third and sixth respectively of the total reduction in drain current. This figure points to the relatively smaller role of drain-end scattering in comparison to source-end scattering, when  $L_{Ch}$  becomes much larger than  $L_{scatt}$ . Scattering is included only in the channel for both cases.

**Fig. 5:** The solid lines represent  $J(Y, E)$  for  $Y$  equal to -17.5, -12.5, -7.5, -2.5, 2.5, 7.5, 12.5 and 17.5 nm, from left to right respectively. The dashed lines represent the first resonant level ( $E_1$ ) along the channel. The dotted lines represent the first moment of energy (mean) with respect to the current distribution function  $J(Y, E)$ , which is  $\frac{\int dE E J(Y, E)}{\int dE J(Y, E)}$ . (a) and (b) correspond to  $L_{scatt} = 11$  and 2.2 nm respectively in device B. Scattering is included every where in the channel. (a) and (b) correspond to the  $Y_{R-Scatt} = 12.5$  nm data points of the dashed and solid lines of Fig. 4. Scattering is included everywhere in the channel but not in the extension regions.

**Fig. 6:** Electrostatic potential versus  $Y$  for device B. Scattering from -12.5 nm to 2.5 nm causes a large change in the source injection barrier ( $E_b$ ). Scattering to the right of 2.5nm causes a much smaller change in  $E_b$ . In the absence of scattering, the potential profile in the channel tends to flatten. The potential drop (or  $E_1$ ) along the channel is more ohmic / linear in the presence of scattering.

**Fig. 7:**  $I_D$  versus  $Y_{R-Scatt}$  for device A with scattering present only in the drain extension region from 5 nm to 30 nm. The large reduction in drain current is due to scattering of hot carriers from the drain extension region back in to the channel. The physics of this effect is completely different from 'classical series resistance' in MOSFETs, which is a much smaller effect. The results obtained from the 'series resistance' and 'scattering calculations' (this paper) are indicated by the arrows. The electron-phonon scattering time is five times larger than in Fig. 2. Inset: Drain current versus drain voltage in the ballistic limit, showing the drain current estimate from the series resistance picture and from our calculation.

	Device A	Devic B
$\tau_{\text{scatt}}$ at source-end (s)	5.0 E-14	5.0E-14 (1.0 E-14)
$\tau_{\text{scatt}}$ at drain-end (s)	2.5 E-14	2.4 E-14 (4.8 E-15)
$\tau_{\text{transit}}$ at $E_b+26$ meV (s)	2.6 E-14	6.4 E-14
$\tau_{\text{transit}}$ at 60 meV (s)	2.0 E-14	5.6 E-14
$v$ at $Y_b$ , $E_b+26$ meV (m/s)	2.2 E+5	2.2 E+5
$v$ at $Y_b$ , 60 meV (m/s)	3.5 E+5	2.8 E+5
$L_{\text{Ch}}$ (nm)	10	25
$v^*(\tau_{\text{scatt}} \text{ at } Y_b)$ $E=E_b+26\text{meV}$ (nm)	11	11 (2.2)
<ul style="list-style-type: none"> <li><math>\tau_{\text{scatt}}</math> – scattering time (<math>\hbar/2\text{Im}(\Sigma^f)</math>)</li> <li><math>\tau_{\text{transit}}</math> - shortest semiclassical transit time for electron with a given total energy = integral <math>\int dy / [2(E-V(y))/m]^{1/2}</math></li> <li><math>v</math> - semiclassical velocity at <math>y = [2(E-V(y))/m]^{1/2}</math></li> <li>For Device B, quantities in brackets are for the case of five times larger scattering rate</li> </ul>		

TABLE I

ESTIMATES OF SCATTERING TIME, TRANSIT TIME, VELOCITY AND SCATTERING LENGTH.

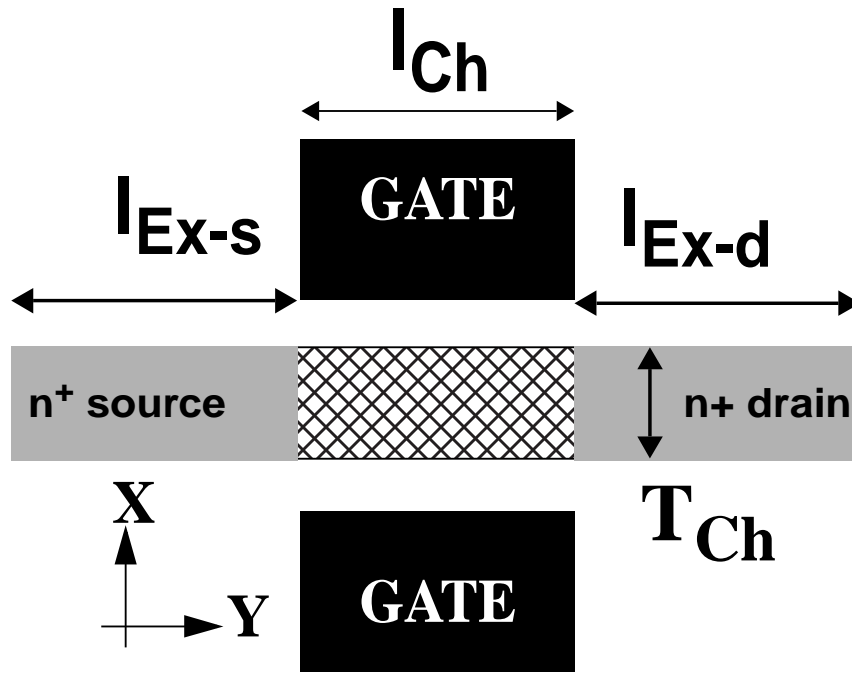


Fig. 1

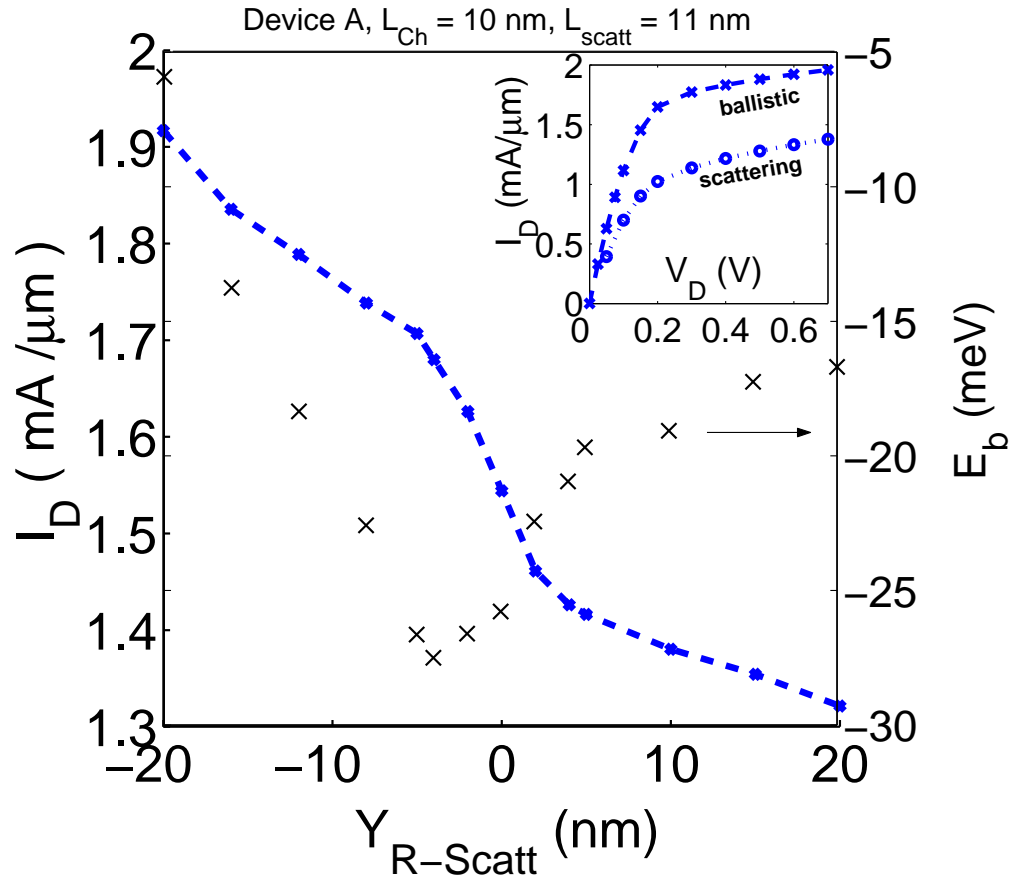


Fig. 2

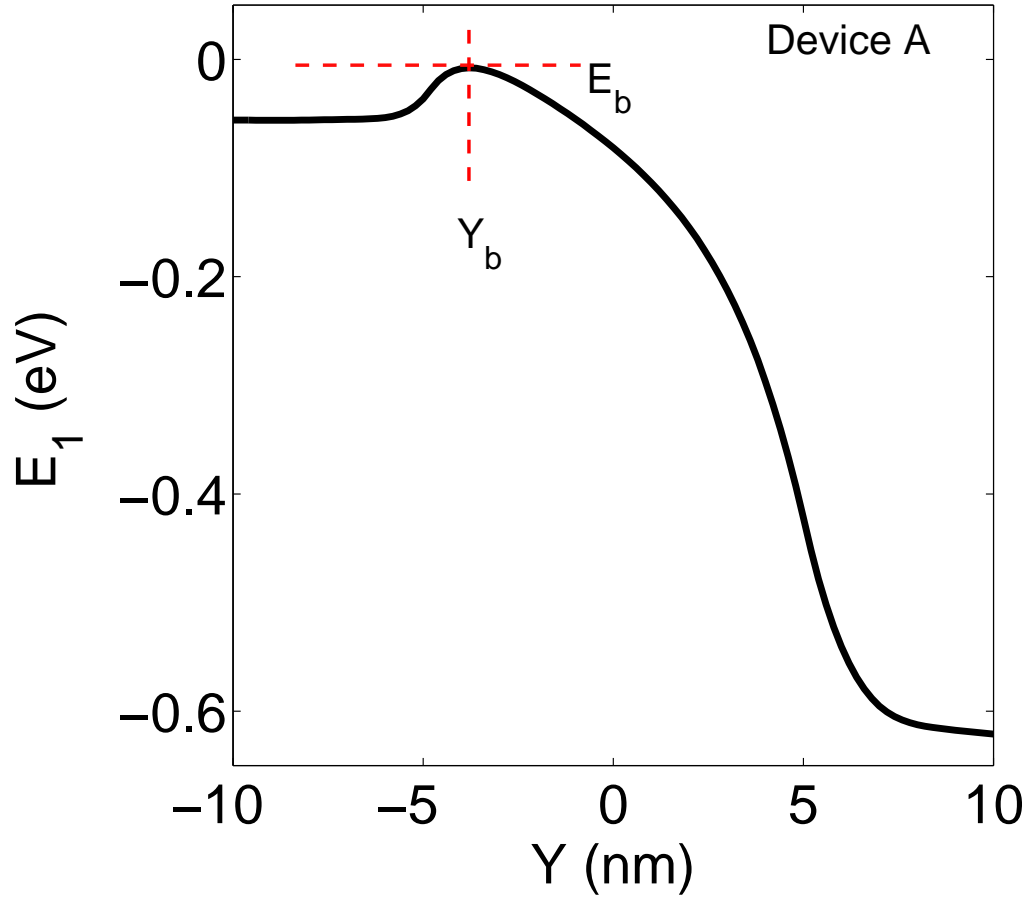


Fig. 3

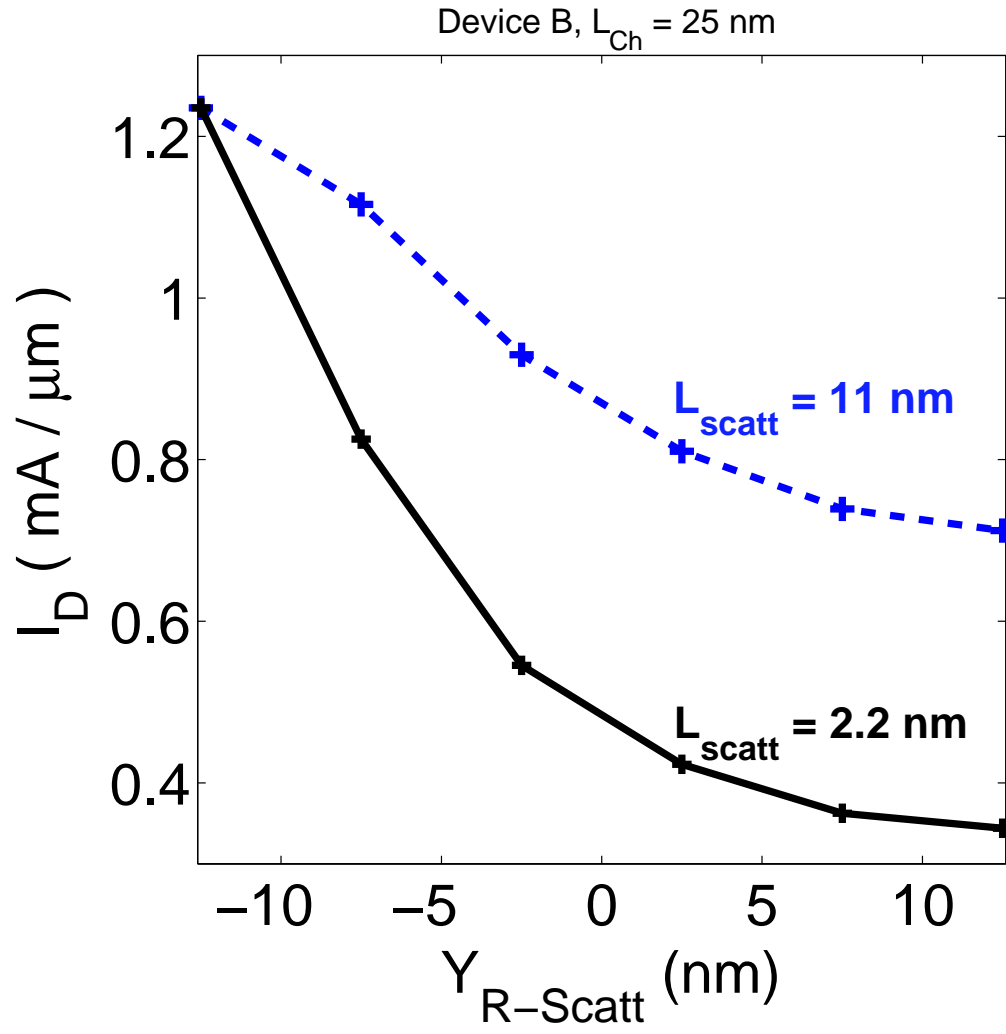


Fig. 4



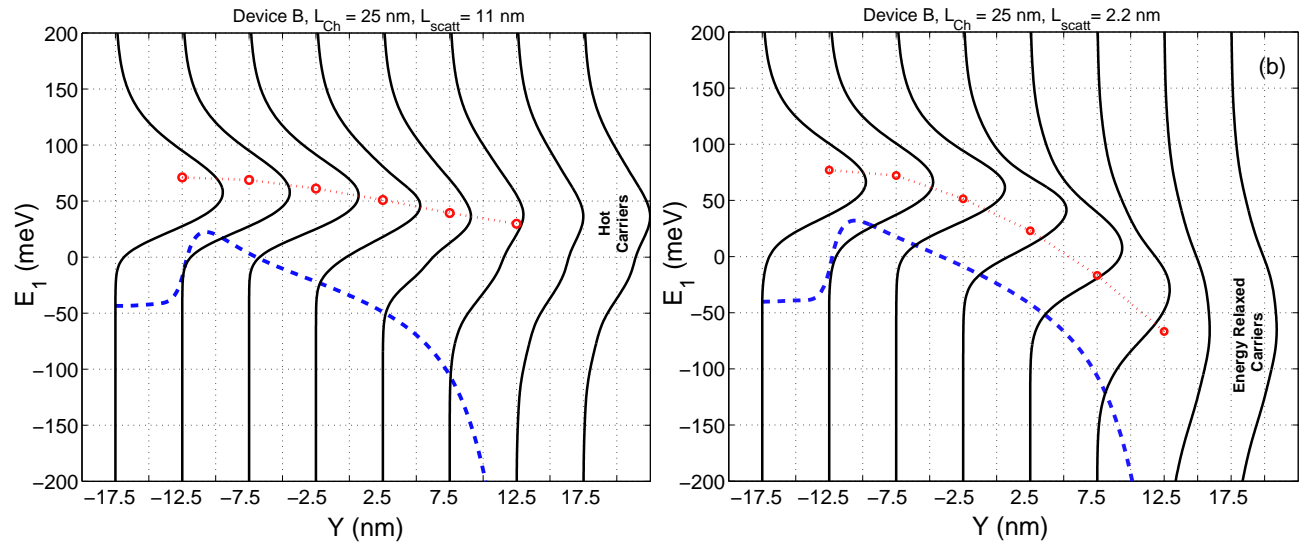


Fig. 5

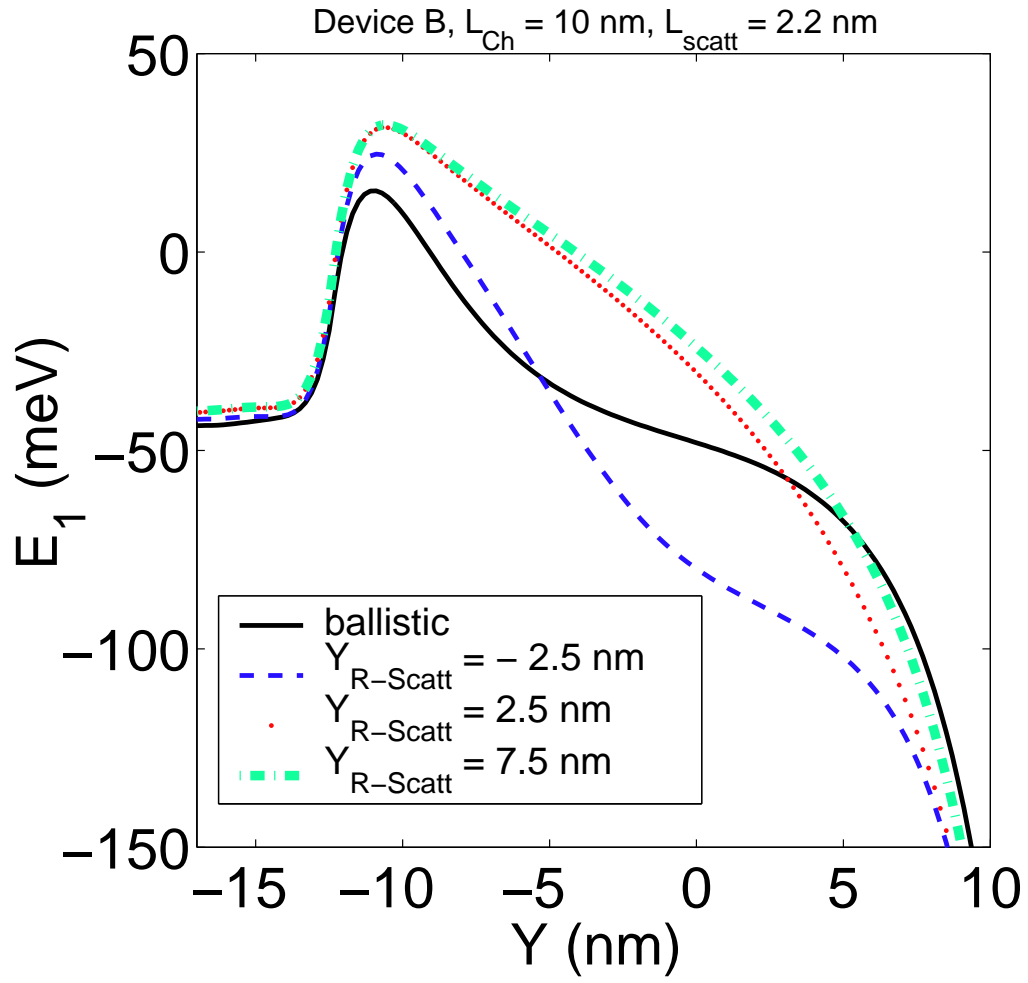


Fig. 6

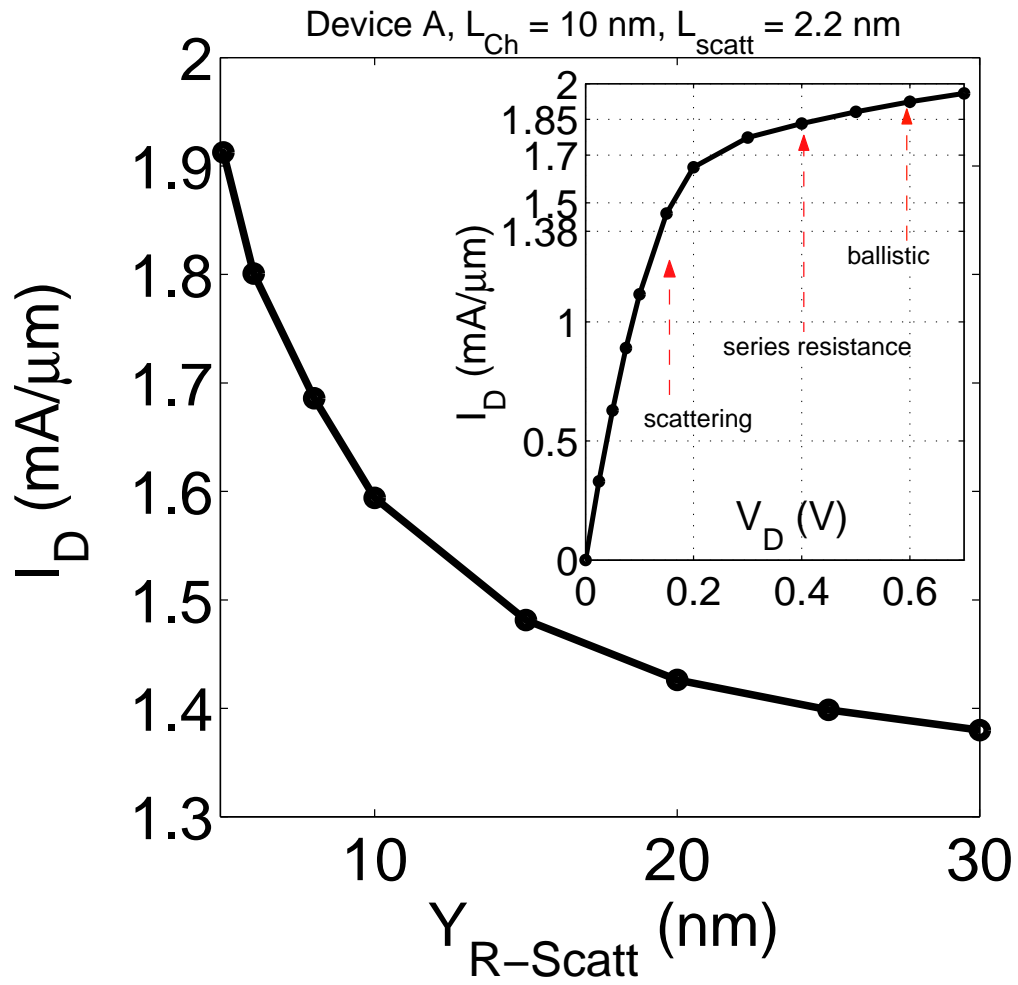


Fig. 7